A Large Population of Obscured AGN in Disguise as Low-luminosity AGN in Chandra Deep Field South

Erini L. Lambrides[1] , Marco Chiaberge[1,2] , Timothy Heckman[1] , Roberto Gilli[3] , Fabio Vito[4,5] , and Colin Norman[1,2]

[1] Department of Physics & Astronomy, Johns Hopkins University, Bloomberg Center, 3400 North Charles Street, Baltimore, MD 21218, USA
[2] Space Telescope Science Institute, 3700 San Martin Drive Baltimore, MD 21218, USA
[3] INAF–Osservatorio di Astrofisica e Scienza dello Spazio di Bologna, Via P. Gobetti 93/3, I-40129, Bologna, Italy
[4] Instituto de Astrofísica and Centro de Astroingeniería, Facultad de Física, Pontificia Universidad Católica de Chile, Casilla 306, Santiago 22, Chile
[5] Chinese Academy of Sciences South America Center for Astronomy, National Astronomical Observatories, CAS, Beijing 100012, People's Republic Of China

Received 2019 September 25; revised 2020 May 6; accepted 2020 May 9; published 2020 July 15

Abstract

Population synthesis models of actively accreting supermassive black holes (or active galactic nuclei (AGN)) predict a large fraction that must grow behind dense, obscuring screens of gas and dust. Deep X-ray surveys are thought to have provided the most complete and unbiased samples of AGN, but there is strong observational evidence that a portion of the population of obscured AGN is being missed. In this paper, we use a sample of AGN derived from the deepest X-ray survey to date, the Chandra 7 Ms GOODS-South Survey, to investigate the nature of low-flux X-ray sources. We make full use of the extensive multiwavelength coverage of the GOODS-South field and cross-match our objects with wavelengths from the radio to the IR. We find that the low X-ray flux AGN in our sample have X-ray luminosities that indicate low-luminosity AGN classification, while their radio, IR, and optical counterparts indicate moderate to powerful AGN classification. We find that the predicted column densities are, on average, an order of magnitude higher than the calculated column densities via X-ray detections for X-ray-faint sources. We interpret our results as evidence of obscured AGN disguised as low-luminosity AGN via their X-ray luminosities. When we compare the estimation of the obscured AGN space density with and without these objects, we find a difference of 40% in the lowest X-ray luminosity regime probed by our sample.

Unified Astronomy Thesaurus concepts: Active galactic nuclei (16); AGN host galaxies (2017); Active galaxies (17); X-ray active galactic nuclei (2035); Optical observation (1169); Infrared sources (793); Extragalactic radio sources (508); Surveys (1671)

1. Introduction

Theoretical models of galaxy formation predict that massive galaxies should have high star formation rates and larger gas reservoirs than what is observed. It has been postulated that actively accreting supermassive black holes (SMBHs), known as active galactic nuclei (AGN), can inject energy into the gas and expel it and/or prevent it from cooling and collapsing into stars through a mechanism called feedback (e.g., Bower et al. 2006; Croton et al. 2006; Heckman & Best 2014). The ubiquity of SMBHs in the center of galaxies and the large energy release per gram of matter accreted onto the SMBH makes AGN feedback the most promising star formation regulation mechanism. Furthermore, star formation and SMBH growth have similar evolutionary tracks (see, for a review, Madau & Dickinson 2014). Theory suggests that feedback from growing SMBHs/AGN is able to successfully reproduce the properties of local massive galaxies (see Silk & Mamon 2012, for a review) and explain the observed galaxy scaling relations and the quenching of star formation in massive galaxies (e.g., Silk & Rees 1998; Fabian 1999; King 2003; Hopkins et al. 2006; Weinberger et al. 2018).

Some models of galaxy evolution and AGN feedback explain the observed scaling relations between SMBHs and galaxy host properties via a merging scenario. In these scenarios, AGN are triggered due to the gravitational torques produced as a result of the merger funneling gas to the central parsecs of the galaxy. A key component of these models is that the majority of SMBH growth is occurring behind large column densities, $N_H > 10^{23}$ cm^{-2} (e.g., Cattaneo et al. 2005; Hopkins et al. 2008; Blecha et al. 2018). These obscured

sources are inherently difficult to observe, but their relative contribution to the total number of AGN can be estimated via AGN synthesis models for the cosmic X-ray background (e.g., Comastri et al. 1995; Gilli et al. 2001; Treister & Urry 2005; Gilli et al. 2007; Akylas et al. 2012; Ananna et al. 2019). Directly observing obscured AGN is possible, but emission at wavelengths less than 2 μm is significantly attenuated by the obscuring material. Over a wide range of energies (i.e., 0.2–200 keV), X-ray observations are thought to provide one of the most reliable methods of selecting AGN and estimating the amount of obscuration (e.g., Brandt & Hasinger 2005; Xue et al. 2011; Liu et al. 2017); however, this is not always true, as Comastri et al. (2011) and Donley et al. (2012) showed that even some of the deepest X-ray surveys miss a substantial fraction of heavily obscured objects.

Obscured AGN can also be identified in the mid-IR (MIR) due to the reprocessing of the obscured UV emission (e.g., Lacy et al. 2004; Houck et al. 2005; Weedman et al. 2006; Yan et al. 2007; Polletta et al. 2008; Stern et al. 2012a; Mateos et al. 2013; Yan et al. 2013). As noted in Hickox & Alexander (2018), color–color diagnostics may provide high completeness but only modest reliability due to sources not always having a prominent AGN component. Thus, AGN hosted in strongly star-forming galaxies may not be identified. This limitation is compounded by the fact that at high redshifts ($z > 2$), star formation and AGN activity peak. Aside from AGN identification, disentangling obscured versus unobscured AGN from MIR colors alone is challenging due to the similarity between these two classes of AGN in their MIR SEDs (e.g., Buchanan et al. 2006; Mateos et al. 2012; Asmus et al. 2014; Hickox et al. 2017); thus, the

combination of large and deep MIR and X-ray surveys is needed to build a large, statistically robust sample of obscured AGN.

The deepest X-ray survey to date is the Chandra Deep Field South (CDFS) survey, which was centered on the GOODS-S region. Due to the severe amount of Compton scattering and absorption that attenuates the X-ray emission at the lower X-ray energies probed by Chandra, data at other other wavelengths must be used to quantify the level of potential AGN obscuration. The obscuring medium that absorbs the X-ray continuum photons reradiates the energy at MIR wavelengths. The combination of X-ray and IR data has been critical in estimating the amount of obscuration in X-ray surveys with energies <10 keV (e.g., Daddi et al. 2007; Donley et al. 2008; Fiore et al. 2009). Many studies using X-ray-selected AGN select AGN as objects with measured luminosities of $L_X > 10^{42}$ erg s^{-1} to avoid contamination from galaxies for which the X-ray luminosity is dominated by star formation. To fully understand the AGN population, it is essential to properly account for the possibility that sources with low observed X-ray luminosity may in fact be moderately to heavily obscured. In this paper, we investigate the nature of these low-luminosity sources.

In Section 2 we describe the data acquisition and sample properties. In Section 3 we present comparisons between the X-ray, radio, IR, and optical counterparts. In Section 4 we discuss the implications of the existence of these sources in two different examples, and we summarize our findings in Section 5. We use an $h = 0.7$, $\Omega_m = 0.3$, $\Omega_\Lambda = 0.7$ cosmology throughout this paper. We use the k-sample Anderson–Darling mid-rank statistic to test the null hypothesis that two samples are drawn from the same population and report the test statistic (D_{ADK}) significance level at which the null hypothesis for the provided samples can be rejected.

2. Sample Selection

The sample discussed in this paper is derived from the deepest X-ray survey to date, the 7 Ms exposure CDFS survey, which covers a total area of 484.2 arcmin^2 (Luo et al. 2017, hereafter L17). The 7 Ms CDFS catalog contains 1008 sources analyzed in three energy regimes: 0.5–7.0 keV (full), 0.5–2.0 keV (soft), and 2–7 keV (hard). We select 523 CDFS sources that have redshifts >0.5, were detected in both the full band and hard band, and are labeled as AGN in the L17 catalog. We use the criterion of $z > 0.5$ to maximize the selection of objects in an epoch where we expect the greatest evolutionary effects. In L17, the sources are classified as AGN if they fulfill one of the photometric and/or spectroscopic criteria as follows.

(a) A source with intrinsic luminosity $L_{0.5-7.0\,keV} \geqslant 3 \times 10^{42}$ erg s^{-1}.

(b) A source with $\Gamma \leqslant 1.0$, where Γ is the effective photon index and a value of $\leqslant 1.0$ is indicative of an obscured AGN.

(c) A source with an X-ray–to–optical flux ratio of log $(f_X/f_R) > -1$, where the X-ray flux is the full band (FB) and the R flux is provided in L17.

(d) A source with a factor of 3 or more X-ray emission over the level expected from pure star formation as traced by the rest radio 1.4 GHz luminosity (Alexander et al. 2005).
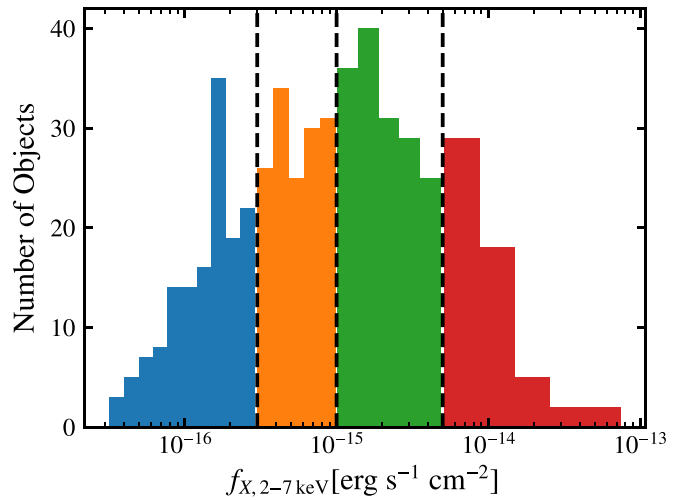

Figure 1. Hard X-ray flux distribution of our sample. The distribution is split into four bins. The color definitions remain consistent throughout this paper.

(e) A source with broad emission and/or high-excitation emission lines in the optical spectrum via the cross-matched spectroscopically identified AGN catalog in Szokoly et al. (2004), Mignoli et al. (2005), and Silverman et al. (2010).

(f) A source with an X-ray–to–near-IR (NIR) flux ratio log $(f_X/f_{K_s}) > -1.2$.

As noted in Xue et al. (2011) and L17, the above criteria are effective but not complete in identifying AGN. In particular, these selection methods may not capture the lowest luminosity or most obscured AGN. Thus, there may be a fraction of sources classified as "galaxies" in L17 that in actuality host an AGN. For the scope of this paper, we present our results on the galaxies classified as AGN-only but explore the objects classified as "galaxies" in the Discussion.

We split the sample into four measured hard X-ray flux bins:

1. $f_{X,2-7\,keV} < 3 \times 10^{-16}$ erg s^{-1} cm^{-2};
2. 3×10^{-16} erg s^{-1} cm$^{-2} \leqslant f_{X,2-7\,keV} < 1 \times 10^{-15}$ erg s^{-1} cm^{-2};
3. 1×10^{-15} erg s^{-1} cm$^{-2} \leqslant f_{X,2-7\,keV} < 5 \times 10^{-15}$ erg s^{-1} cm^{-2}; and
4. $f_{X,2-7\,keV} \geqslant 5 \times 10^{-15}$ erg s^{-1} cm^{-2}.

The values of the first three bins were chosen to contain roughly equal numbers of objects and correspond to the flux limits of other X-ray surveys in this field. The highest flux bin contains roughly 50 objects. The values of 3×10^{-16} and 1×10^{-15} erg s^{-1} cm^{-2} correspond to the flux limit at 50% sky coverage for the Chandra 4 Ms 2–8 keV (Xue et al. 2011) and XMM 3.45 Ms GOODS-S 2–10 keV (Ranalli et al. 2013) surveys, respectively. We show the distribution of the hard X-ray flux values as presented in L17 and the bin definitions used throughout this paper in Figure 1.

Since the main focus of this paper is to understand the nature of the low-flux sources in the context of AGN classification, we choose the highest-energy X-ray band available because it should be least affected by obscuration and thus a more accurate indicator of the intrinsic AGN power. Furthermore, we apply an estimate of the intrinsic absorption as derived by L17 to the hard X-ray flux values. The hard X-ray band fluxes as
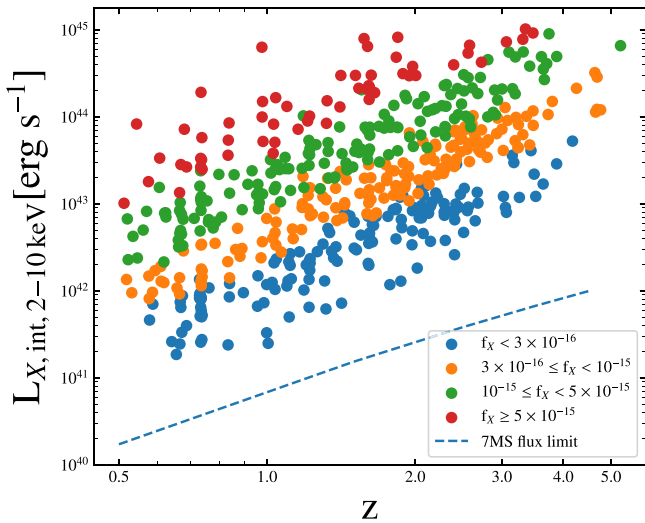
Figure 2. Redshift vs. absorption-corrected or intrinsic X-ray luminosity. The median and mean redshifts for our sample are 1.6 and 1.7, respectively. The points are color-coded by their flux bin. The blue dashed line corresponds to the mean Chandra 7 Ms flux limit (Luo et al. 2017).

presented in L17 are not absorption-corrected, but L17 provided an estimate of the intrinsic absorption that they apply to their full band luminosities as follows.

The X-ray spectrum of an AGN can be described by a power law: the photon number density takes the form $N(E) \sim E^{-\Gamma}$, where Γ is the photon index and E is the photon energy. In L17, they estimate the power-law photon index Γ_{eff} from the hard-to-soft band ratios, where Γ_{eff} includes Galactic absorption. Then, L17 uses the Portable, Interactive, Multi-Mission Simulator (PIMMS; Mukai 1993) to estimate the intrinsic absorption. By assuming that the intrinsic power-law spectrum has a fixed photon index of 1.8 modified by Galactic absorption, any smaller value is likely caused by intrinsic absorption (N_H). We then use the estimated N_H tabulated in L17 to derive the intrinsic hard X-ray luminosity. Finally, we use PIMMS to recalculate the intrinsic hard X-ray luminosities over the rest 2–10 keV energy band, which we define as $L_{X,int,2-10\,keV}$. We modify the energy band so that our work may be directly comparable to similar studies. In Figure 2, we show the $L_{X,int,2-10\,keV}$ values as a function of redshift. The points are color-coded by their flux bin. The blue dashed line corresponds to the mean Chandra 7 Ms flux limit derived in L17, 3.6×10^{-17} erg s^{-1} cm^{-2}, recalculated over the 2–10 keV energy range. In the following sections, we describe the collection of the multiwavelength data we use in this work, with the aim of investigating the nature of the low-flux X-ray AGN sources.

2.1. IR Measurements

We cross-match our X-ray sample to IR catalogs to quantify the effect of varying levels of obscuration on our X-ray fluxes. We use Spitzer Infrared Array Camera (IRAC) 3.4, 4.5, 5.8, and 8.0 μm data; the Spitzer peak-up imager (PUI) on the Infrared Spectrograph (IRS) instrument (Houck et al. 2005) 16 μm data; Multi-band Imaging Photometer for Spitzer (MIPS) 24 μm data; and Herschel Photodetector Array Camera and Spectrometer (PACS) 100 and 160 μm data. The Spitzer IRAC and Herschel data were taken from the GOODS-Herschel survey catalog, where Herschel flux densities and

uncertainties were obtained from point-source fitting using Spitzer 24 μm detection positions as a prior (Elbaz et al. 2011). The optical counterparts to the CANDELS + 3DHST combined catalog (Skelton et al. 2014) were provided by L17. We cross-match our sources to the Elbaz et al. (2011) catalog, which also provided associated GOODS counterpart coordinates, using the optical counterpart coordinates with a 1″ search tolerance. The Spitzer IRS PUI 16 μm detections were also found using the optical counterpart coordinates with a 1″ cross-match search tolerance to the 16 μm GOODS-S catalog (Teplitz et al. 2011). We find 169 (32.3%) X-ray source matches in all four IRAC bands and MIPS 24 μm and 124 (24%) matches in Spitzer IRS PUI 16 μm data, and 76 (14.5%) and 62 (11.9 %) objects have PACS 100 and 160 μm detections, respectively. We note that the majority of the analysis in Section 3 is constrained to X-ray sources with IRAC bands and MIPS 24 μm detections. Within this X-ray MIR subsample, over 50% of objects have both Herschel detections.

2.2. Optical Measurements

Another probe of AGN power is the strength of high-ionization optical lines. The counterparts to the CANDELS + 3DHST combined catalog (Skelton et al. 2014) were provided by L17. We use these coordinates from the L17 catalog to perform a cross-match with a 0″.2 tolerance to the rest-frame color catalog (Skelton et al. 2014), emission line catalog (Momcheva et al. 2016), and ACS/WFC3IR images (Skelton et al. 2014). We have overlap with 167 objects with >5σ detections with ACS F435W photometry and 253 objects with >5σ detections with WFC3IR F160W photometry. In the emission line catalog, we have 40 objects with >2σ [O III] detections.

2.3. Radio Measurements

Radio emission is present in both AGN- and star formation–dominated galaxies. The L17 catalog provides 1.4 GHz fluxes via the Very Large Array (VLA) survey centered on the CDFS field. We find 94 objects above the 5σ flux density limit of 37 μJy. For the detected objects, we use the redshifts provided in L17 and calculate the rest-frame luminosity for each object assuming a radio spectral index of $\alpha = 0.8$, where α is defined as $f_\nu \propto \nu^{-\alpha}$. For the undetected objects, we calculate the upper limit using the limiting flux of the GOODS-S VLA survey (Miller et al. 2013) from which the upper limit fluxes are derived. In Figure 3, we show a summary of all of the cross-matching results of our L17 subsample with the other wavelengths.

3. Results

3.1. X-Ray and Rest-frame 5 μm Continuum

As stated in Section 1, the combination of hard X-ray and MIR data offers one of the best probes of obscuration in AGN host galaxies. One of the most unambiguous signatures of AGN activity is X-ray emission, and in obscured AGN, the material that attenuates the X-ray emission is expected to emit in the MIR. A measurement of a bright, unobscured source in both the X-ray and MIR allows for empirical relationships to be derived between these quantities. The MIR contains features that can be attributed to AGN and/or star formation (SF) processes. Between 3.2 and 5.7 μm, AGN torus emission
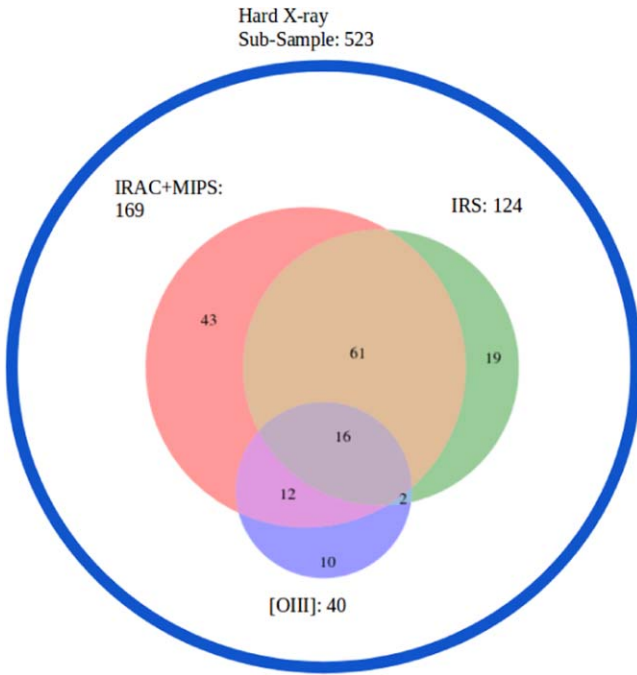
Figure 3. Cross-match summary. After selecting all of the sources from Luo et al. (2017) that have $z > 0.5$ full and hard band detections and are classified as AGN via their catalog (as represented by the large blue circle), we then present the summary of the cross-matching statistics of these 486 objects to the IR and optical data used in Section 3.

dominates over MIR SF processes (Nenkova et al. 2008; Kirkpatrick et al. 2012; Lambrides et al. 2019). Previous studies have used spectral energy distribution (SED) decomposition or templates to calculate the rest-frame emission in this region (Mullaney et al. 2012; Stern 2015). Due to the uncertainties introduced with these methods, we instead take advantage of our large sample and its multiwavelength properties.

We infer the rest-frame 5 μm continuum region luminosities to directly measure the emission in this spectral region. For regions of redshift where $0.5 < z \leqslant 1.5$, $1.8 < z \leqslant 3.1$, and $z \geqslant 3.1$, we use the observed IRAC 8 μm, IRS PUI 16 μm, and MIPS 24 μm luminosities, respectively. This corresponds to rest-frame luminosities in the 3.2–5.7 μm continuum region, depending on the object's redshift, and we refer to these luminosities as L_{Torus^*} for simplicity. We use the nomenclature Torus* because, although we are not estimating the entirety of the IR torus luminosity, we expect the AGN torus luminosity to dominate over SF processes in this wavelength regime.

We test the prediction of the AGN torus luminosity dominating the flux emission in the wavelengths used to calculate the L_{Torus^*} values on a local AGN and starburst sample. Lambrides et al. (2019) uniformly analyzed all AGN and SF galaxies ever observed with the Spitzer IRS (Houck et al. 2004). As similar studies have shown, Lambrides et al. (2019) found that, even for low-luminosity ($L_{24\mu\mathrm{m}} < 10^{42}$ [erg s^{-1}]) AGN, the polycyclic aromatic hydrocarbon (PAH) 6.2 μm equivalent width (EQW) is an excellent indicator of AGN contribution to the MIR: the lower the 6.2 μm EQW, the more the spectrum is dominated by an AGN component. The EQW classifier was able to separate highly star-forming ultraluminous infrared galaxies with and without an AGN. Using the spectra and other cross-matched data provided in Lambrides et al. (2019), we calculate L_{Torus^*} using the same

approach as in this work. We find that L_{Torus^*} is as good as the 6.2 μm classifier. Performing a Spearman rank correlation on L_{Torus^*} (normalized by K-band luminosity to account for mass difference) and PAH 6.2 μm EQW, we measure an anticorrelation (p-value < 0.001). As an additional check, we used the EQW to estimate the $L_{5\mu\mathrm{m}}$ from the AGN component alone or $L_{5\mu\mathrm{m},\mathrm{AGN}}$, which is defined as $L_{5\mu\mathrm{m}} \times (1.0–0.54/\mathrm{EQW})$. Here $L_{5\mu\mathrm{m}}$ is derived from the spectra and is an integrated quantity between rest-frame 4.8 and 5.2 μm. The factor of $(1.0–0.54/\mathrm{EQW})$ is set to equal 1 when the EQW > 0.54, for this represents that 100% of the emission is being powered by SF (see Armus et al. 2007; Petric et al. 2011; Stierwalt et al. 2014, for details of EQW to MIR AGN power estimates). We find a 0.1 dex agreement between the $L_{5\mu\mathrm{m},\mathrm{AGN}}$ values and the L_{Torus^*} values. The only region of the parameter space where L_{Torus^*} may fail is in objects where L_{Torus^*} is completely dominated by SF. However, such objects would cluster around the solid orange line in Figure 7, which we do not observe.

We show the relationship between L^*_{Torus} and $L'_{\mathrm{X,int,2-10\,keV}}$ in Figure 4. The blue solid line is the luminosity-dependent, absorption-corrected X-ray $\nu L_\nu(6\,\mu\mathrm{m})$ relationship from Stern (2015, hereafter S15), which parameterizes the relationship as $\log L(2\text{–}10\mathrm{keV}) = 40.981 + 1.024x - 0.047x^2$, where $x \equiv \log(\nu\,L_\nu(6\,\mu\mathrm{m}))$. We chose the S15 relation due to the similar method in which they derived the equivalent L_{Torus^*} luminosity and the large luminosity range their sample covers. We find that over 90% of our objects with the lowest X-ray fluxes, $f_{\mathrm{X},2-7\,\mathrm{keV}} < 10^{-16}$ erg s^{-1} cm^{-2}, are $\geqslant 2\sigma$ below the S15 relation. We compute the Anderson–Darling statistic to test whether the lowest flux bin is drawn from the same population of $L'_{\mathrm{X,int,2-10\,keV}}$ to L^*_{Torus} values from the rest of the flux bins, and we find that the null hypothesis can be rejected ($D_{\mathrm{ADK}} = 43.7$, critical value (1%) $= 6.546$, significance $= 0.001$). The teal, pink, and gray triangles are the IRAC, IRS PUI, and MIPS upper limits, respectively. We calculate the upper limits using the flux limits provided for the relevant MIR wavelength used in the L_{Torus^*} calculation. The flux limit for observed IRAC 8 μm, IRS PUI 12 μm, and MIPS 24 μm is 1.6, 65, and 20 μJy, respectively. We test the effect of upper limits by performing a censored regression analysis on each X-ray flux bin, and we find that the L_{Torus^*} and $L'_{\mathrm{X,int,2-10\,keV}}$ relationship in each flux bin remains unchanged when upper limits are taken into account.

The tension between the X-ray and L_{Torus^*} for the lowest X-ray flux objects suggests that the low X-ray flux objects are (i) intrinsically weak AGN with a non-AGN component contributing to the MIR luminosity or (ii) moderately to heavily obscured AGN. With regards to scenario (i), any non-AGN component in these systems would most likely arise from SF processes. In Section 3.2, we compare the X-ray emission to a direct probe of AGN power that can be less affected by obscuration as compared to the X-rays: the [O III] $\lambda5007$ luminosity. In Section 3.3 we test whether the excess MIR emission for the lowest flux sources can be attributed to a low-luminosity AGN in a host galaxy with extreme amounts of SF.

3.2. X-Ray and [O III] $\lambda5007$ Luminosities

The luminosity of emission lines formed in the narrow-line region, such as [O III] $\lambda5007$, can be used as a quasi-isotropic indicator of AGN power (Brinchmann et al. 2004; Heckman et al. 2005; LaMassa et al. 2010). One of the strongest narrow forbidden lines, [O III] $\lambda5007$ is emitting in a region far from
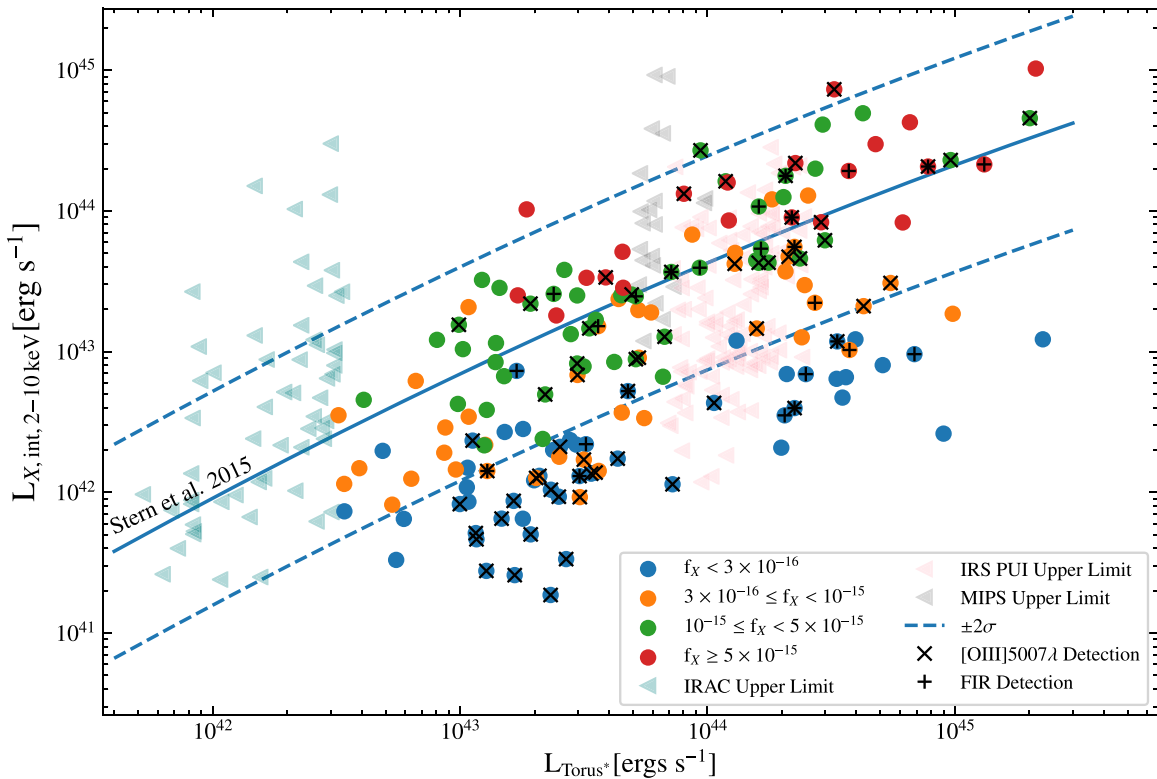
Figure 4. Shown is L_{Torus^*} vs. $L_{X,int,2-10\,keV}$. We calculate the rest-frame L_{Torus^*} values by splitting the sample into bins of redshift and using the observed IR flux that corresponds to a rest-frame flux between 3.4 and 5.7 μm. The points are color-coded by X-ray flux. The blue solid line is the luminosity-dependent relationship from S15. The dashed blue lines are the 2σ dispersion from the Marchesi et al. (2016) sample. The gray triangles are the MIR upper limits. Objects overlayed with an X symbol have a 2σ or greater [OIII]5007λ detection. Objects overlayed with a + symbol have a 5σ or greater Herschel 100 micron detection.

the dusty torus. We check whether a robust optical line indicator of AGN power is consistent with the X-ray emission of our objects. The [O III] λ5007 feature may be attenuated due to either nuclear or host-galaxy obscuration. Thus, without correction, an observed [O III] λ5007 luminosity may be thought of as a lower limit. Using the [O III] fluxes derived from HST grism spectroscopy provided in Momcheva et al. (2016), we compare the calculated [O III] luminosities to $L_{X,int,2-10\,keV}$ in Figure 5. In Figure 5, we also plot the relationship of L[O III] λ5007 versus $L_{X,int,2-10\,keV}$ for a sample of optically selected type 1 AGN (Yan et al. 2011). Furthermore, for comparison, we additionally plot the type 1 and type 2 AGN sample from Heckman et al. (2005). The Heckman et al. (2005) sample is not corrected for nuclear obscuration. We find that our results from Figure 4 are consistent with Figure 5: 85% of our lowest flux objects are at least 2σ below the Yan et al. (2011) relation and in the same parameter space as the Heckman et al. (2005) type 2 AGN sample. We compute the Anderson–Darling statistic to test whether the lowest flux bin is drawn from the same population of $L'_{X,int,2-10\,keV}$ to L[O III] λ5007 values from the rest of the flux bins, and we find that the null hypothesis can be rejected ($D_{ADK} = 8.30$, critical value (1%) = 6.546, significance = 0.001). The inconsistency between the X-ray and the [O III] emission observed for a substantial fraction of X-ray sources strongly hints at them not being truly low-power AGN. In the next section, we follow up on this hypothesis by checking whether these apparently underluminous X-ray sources have an extra component in the MIR due to an extremely large amount of star formation.

3.3. Do the Low X-Ray Flux Objects Have Significant SF?

Monochromatic continuum luminosity at 24 μm is commonly used to trace star formation due to the warm dust associated with high-mass star-forming regions emitting at this wavelength (Calzetti et al. 2007). On the other hand, SF processes also contribute to the soft and hard X-ray components (Persic & Rephaeli 2002). The X-ray emission in SF galaxies is predominately from gas in the interstellar medium heated by stellar winds and supernova and point sources such as X-ray binaries. For star-forming galaxies, very high IR luminosities ($L_{IR} > 10^{46}$ erg s^{-1}) must be observed in order to correspond to $L_{X,2-10\,keV} > 10^{42}$ erg s^{-1} (Symeonidis et al. 2014). Conversely, for galaxies with an AGN, the 24 μm continuum luminosity may be significantly contaminated with reprocessed light from the central engine. Even more importantly, in AGN, the X-ray emission tightly traces the power of the central engine, unless the central engine is obscured. Thus, the relationship between X-rays and the IR will vary significantly between SF- and AGN-dominated galaxies.

In Figure 6, we show the relationship between $L_{X,int,2-10\,keV}$ and the observed 24 μm luminosities for our sample. The AGN studies quantifying this relation, or using other MIR continuum measurements, find an almost one-to-one relationship between these quantities, with minimal scatter (<1 dex; Gandhi et al. 2009; Asmus et al. 2015). The gray shaded region is the range of values for unobscured AGN adapted from Asmus et al. (2015). The red solid and dashed lines are the X-ray–to–24 μm relationship for SF galaxies and $\pm2\sigma$, respectively, for a sample of $z \sim 1$ SF galaxies from Symeonidis et al. (2014). This relationship is adapted from Symeonidis et al. (2014) by converting the $L_{8-1000\mu m}$ values to 24 μm using the conversion
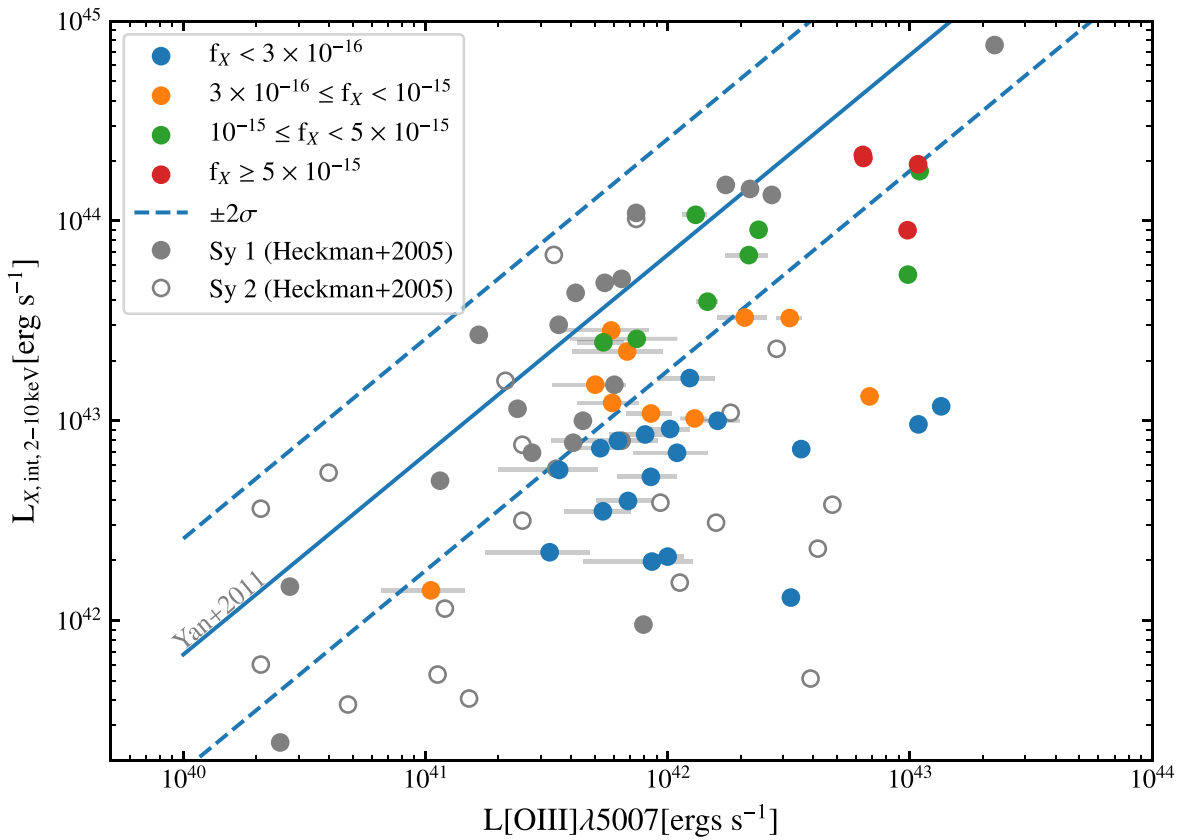
Figure 5. Shown is $L_{X,int,2-10\,keV}$ vs. L[O III] $\lambda5007$. The points are color-coded by $f_{X,2-7\,keV}$. The blue solid line is the relationship parameterized for type 1 AGN in the AEGIS sample (Yan et al. 2011). The error bars are the L[O III] $\lambda5007$ 1σ confidence intervals via Momcheva et al. (2016). The filled and open gray circles are type 1 and type 2 AGN, respectively, from Heckman et al. (2005).

presented in Calzetti et al. (2010). The points are color-coded by redshift, and the points that are circled in red are the lowest flux bin objects. Similarly to what we showed in the previous sections, we see an apparent inconsistency. A significant fraction of the X-ray sources appear to be underluminous with respect to their observed 24 μm luminosity. For the redshift range spanned by our sources, the rest-frame 24 μm wavelength ranges from 6 to 16 μm.

We test whether there is a significant dependence between redshift and location of the points with respect to the Asmus et al. (2015) relation due to our usage of the observed 24 μm fluxes. We quantify the fraction of objects below the Asmus et al. (2015) relation in each redshift bin, and we find for $0.5 < z < 1.0$, 61%; $1.0 < z < 1.5$, 56%; $1.5 < z < 2.0$, 55%; $2.0 < z < 2.5$, 71%; and $z > 2.5$, 21%. For every redshift bin, excluding the highest bin, the fraction of sources 2σ below the Asmus et al. (2015) relation is between 50% and 60%. The lower fraction in the highest redshift bin is most likely due to the difference in sensitivity of the MIPS survey as compared to the 7 Ms survey. In fact, as quantified in Elbaz et al. (2011), a $z \sim 3$ galaxy would need to be at least 1×10^{46} erg s^{-1} in order to be 5σ above the flux limit of 100 μJy in MIPS 24 μm, and our sample does not contain any such objects.

As seen in Figure 6, the objects that deviate the most from the Asmus et al. (2015) parameter space are the low-flux X-ray objects, but they are all at least 4σ above the SF relation. Furthermore, these very same objects are below the canonical X-ray relations with the $L_{\text{Torus}*}$ and optical line emission (see Figures 4 and 5).

In addition, we can directly estimate the contribution SF processes may have to the portion of the SED that $L_{\text{Torus}*}$ probes. A common method used in the literature to diagnose the extent that SF processes power the MIR spectrum is via color-selecting diagnostics (e.g., Lacy et al. 2004; Sajina et al. 2005; Stern et al. 2005; Lacy et al. 2004; Stern et al. 2012a; Assef et al. 2013). A potential issue highlighted in the literature is a substantial fraction of X-ray-selected AGN being missed in the MIR color-based methods of AGN classification. Donley et al. (2012) extensively covered the reliability and completeness of both the IRAC color wedge (Lacy et al. 2004; Stern et al. 2005; Lacy et al. 2007; Stern et al. 2012b) and their own power-law criteria in the context of the X-ray luminosity of their sources. They found that fewer than 20% of $L_{X,int,2-10\,keV} < 10^{43}$ erg s^{-1} sources are selected as AGN via these methods. They inferred that the majority of AGN missed by the IRAC wedge and IRAC power-law criteria are lower-luminosity and/or more heavily obscured AGN. Additionally, the IRAC AGN wedge does not reliably select AGN at higher redshifts. As shown in Kirkpatrick et al. (2013, 2015), some $z > 0.1$ SF galaxies erroneously become selected as AGN as the IRAC bands begin to probe redder wavelengths of the spectrum. In summary, the completeness and reliability issues of color-based methods are exacerbated for the types of objects in our sample: higher-redshift, lower-to-moderate-luminosity AGN. Due to the large multi-wavelength nature of our sample, we can use rest-frame luminosities and directly compare the regions of the SED that are dominated by SF processes to the region $L_{\text{Torus}*}$ probes.

Between 100 and 160 μm, the dust spectrum can be approximated by a power law: $f_\nu \sim \nu^\alpha$. We use the observed
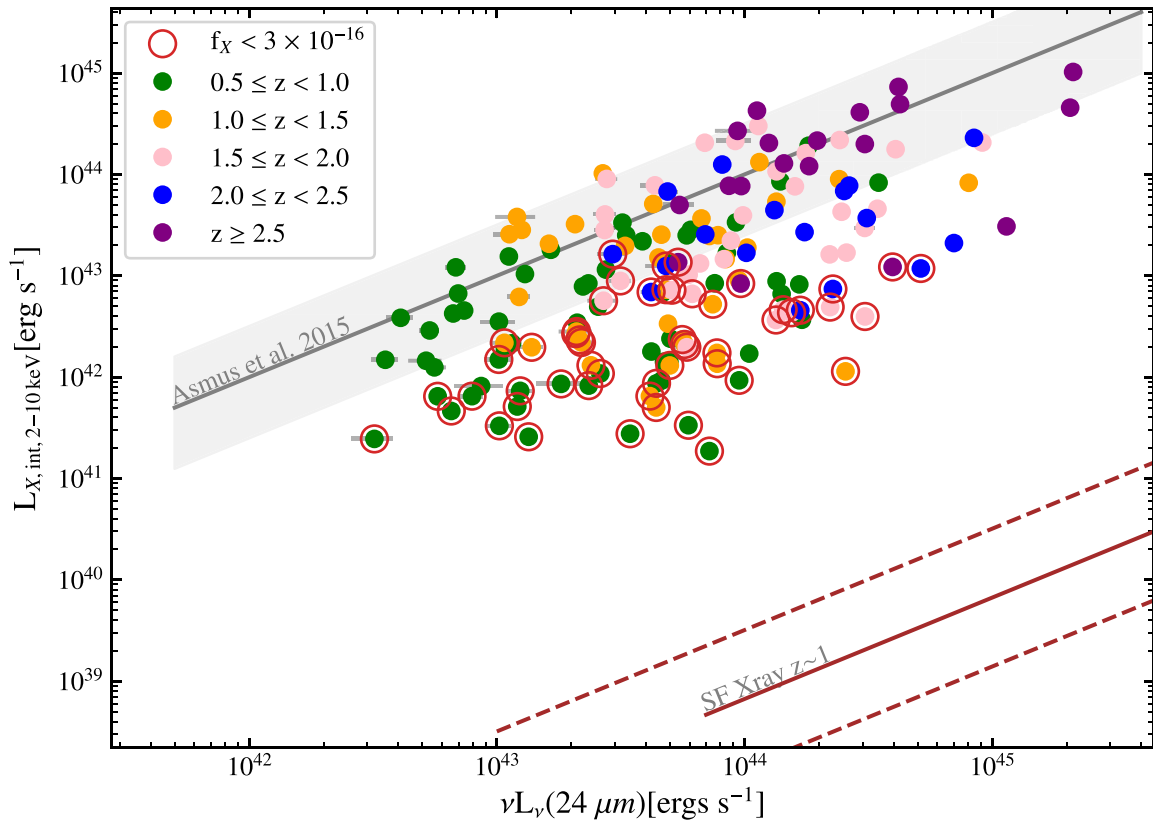
Figure 6. Shown is 24 μm vs. $L_{X,int,2-10\,keV}$. The points are color-coded by redshift. The gray line surrounded by the gray shaded area is the Asmus et al. (2015) relation for nuclear 18 μm and intrinsic 2–10 keV luminosities with the dispersion of values from their sample of unobscured AGN. The red solid and dashed lines are the X-ray–to–24 μm relationship for SF galaxies and $\pm 2\sigma$, respectively, for a sample of $z \sim 1$ SF galaxies from Symeonidis et al. (2014). This relationship is adapted from Symeonidis et al. (2014) by converting the $L_{8-1000\mu m}$ values to the 24 μm luminosity using the conversion presented in Calzetti et al. (2010). The points circled in red indicate objects that are in the lowest X-ray flux bin.

100 and 160 μm to calculate α and extrapolate the 50 μm luminosity. The ratio of $L_{50\mu m}$ to L_{Torus^*} is smaller in galaxies where AGN dominate the 5 μm emission. As shown in Brown et al. (2019), the peak AGN contamination is in the MIR, and redward of 30 μm, the contribution becomes less significant.

We calculate the $L_{50\mu m}$-to-L_{Torus^*} ratios for our sample. In Figure 7, we show the distribution of our values. We also show the ratio for three different MIR AGN templates from Kirkpatrick et al. (2015). An MIR AGN fraction of 1.0 corresponds to a galaxy whose AGN dominates the SED between 5 and 15. As the MIR AGN fraction decreases, the SF contribution in this wavelength regime increases. In Figure 7, the solid, dashed, and dotted red lines correspond to $L_{50\,\mu m}$-to-L_{Torus^*} ratio values for the Kirkpatrick et al. (2015) AGN templates with MIR fractions of 1.0, 0.5, and 0.1, respectively. The solid orange line is the ratio value for the $z \sim 1$ SF galaxy template from Kirkpatrick et al. (2013).

The median $L_{50\mu m}$-to-L_{Torus^*} ratio for our sample is 1.1 and roughly three times smaller than the expected SF value. Our results show that L_{Torus^*} is not significantly contaminated with SF emission. This corroborates the idea that our objects do not host intrinsically weak AGN with a large star-forming component.

3.4. Chandra 7 Ms Total Sample versus Spectrally Constrained Sample

As seen in Sections 3.1 and 3.2, and as will be seen in Section 4.3, the X-ray luminosities derived from simple
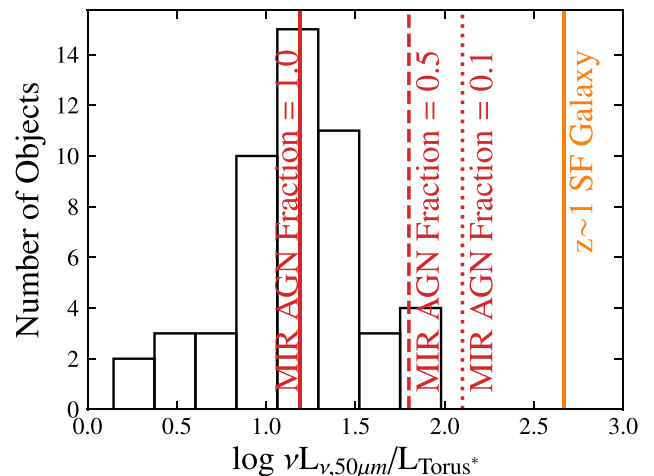

Figure 7. Shown is $L_{50\mu m}$ to L_{Torus^*}. The solid, dashed, and dotted red lines are the ratio values for the Kirkpatrick et al. (2015) templates with MIR AGN fractions of 1.0, 0.5, and 0.1, respectively. The solid orange line is the ratio value for the Kirkpatrick et al. (2012) $z \sim 1$ SF galaxy template.

assumptions are significantly underestimating the intrinsic luminosity of the low-flux sources. On the other hand, Liu et al. (2017) performed a detailed spectral analysis of the X-ray-bright AGN in the Chandra 7 Ms sample. Their objects were selected from L17 only if they were classified as AGN and had at least 80 counts in the hard band. This threshold
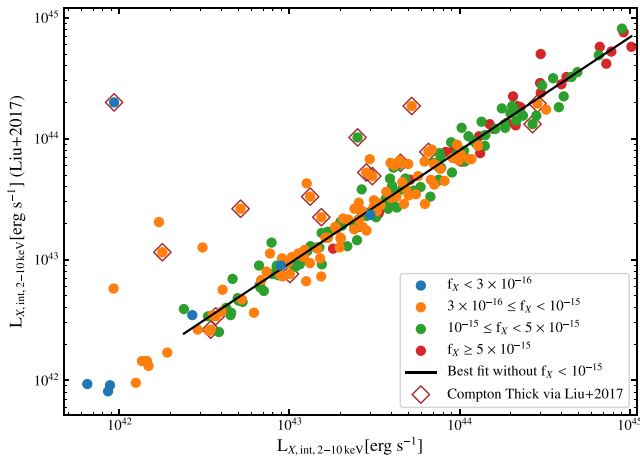
Figure 8. Comparison of our $L_{X,\text{int},2-10\,\text{keV}}$ and Liu et al. (2017) spectrally derived $L_{X,\text{int},2-10\,\text{keV}}$. The blue points are in the lowest X-ray flux bin ($< 3 \times 10^{-16}$ erg s^{-1} cm^{-2}). The black solid line is the best-fit relationship for all of the objects, excluding the two lowest flux bins. The diamonds are the objects spectrally classified as Compton-thick AGN via Liu et al. (2017).

corresponds to a 2–7 keV flux of 2×10^{-16} erg s^{-1} cm^{-2}. They performed a systematic X-ray spectral analysis with an emphasis on constraining intrinsic obscuration. We compare the X-ray properties derived from their 7 Ms subsample to the L17 subsample. In Figure 8, we show a comparison of the $L_{X,\text{int},2-10\,\text{keV}}$ of our sample derived from L17 and the $L_{X,\text{int},2-10\,\text{keV}}$ derived from Liu et al. (2017). The blue points are the lowest X-ray flux bin objects ($< 3 \times 10^{-16}$ erg s^{-1} cm^{-2}). We expect the higher flux bins to be the least affected by the X-ray underestimation in L17 and thus more consistent with the Liu et al. (2017) analysis. Therefore, the black solid line is the best-fit relationship for all of the objects, excluding the two lowest flux bins. Of the 16 objects classified as Compton-thick via Liu et al. (2017) and in our sample, the difference between the $L_{X,\text{int},2-10\,\text{keV}}$ derived in Section 2 and the spectrally derived hard X-ray luminosities is, on average, -0.6 dex. It is important to point out that 44% of these Compton-thick sources are in the lowest X-ray flux bins. We also note that over 78% of the lowest flux objects in the L17 sample were not spectrally analyzed in Liu et al. (2017) due to their low flux counts.

We then compare the Liu et al. (2017) intrinsic hard band X-ray luminosities with $L_{\text{Torus}*}$ in Figure 9. The points are color-coded by the X-ray flux provided in L17. The blue solid line is the luminosity-dependent relationship from S15. Points surrounded by a red diamond are classified as Compton-thick in Liu et al. (2017). The gray points are the $L_{X,\text{int},2-10\,\text{keV}}$ values from Figure 4 that did not have enough X-ray counts to be analyzed in Liu et al. (2017). The Liu et al. (2017) absorption-corrected luminosities bring these objects closer to or within 2σ of the S15 relationship. Thus, when a more sophisticated X-ray analysis is available, the intrinsic absorption estimation yields more accurate luminosities for sources with enough photon counts. The sources in our sample that have the greatest underestimation of X-ray luminosity have insufficient X-ray counts to perform the above spectral analysis. Thus, when X-ray photon statistics are poor, X-ray versus multiband diagnostics are necessary to approximate obscuration.

4. Discussion

4.1. The Nature of Low X-Ray Flux Sources

In Section 3, we find a population of low X-ray flux objects whose physical nature is unclear when taking into account the properties of MIR and optical emission. A classification of these sources based on their X-ray luminosity identifies these objects as low-luminosity AGN. However, when only considering the MIR and optical line emission, the same objects are classified as moderate-to-high-luminosity AGN. More quantitatively, in Section 3.1, we find that 44% are at least 2σ below the expected S15 relationship. Of these objects, 90% are in the lowest X-ray flux bin. In Section 3.2, we find that 85% of our sample has [O III] $\lambda 5007$ luminosities that are $\geqslant 2\sigma$ below their predicted $L_{X,\text{int},2-10\,\text{keV}}$ values via the Yan et al. (2011) relationship. In Section 3.3, we show that the tension between the X-ray luminosities and $L_{\text{Torus}*}$ cannot be explained by an unaccounted-for SF component. Thus, we find strong evidence for a large population of obscured AGN disguising as low-luminosity AGN.

The multiwavelength analysis of this work indicates that over 40% of our sample has underestimated intrinsic obscuration. We note that the lowest flux objects correspond to a mean X-ray luminosity of 2.8×10^{42} [erg s^{-1}]. Although in L17, there are multiple criteria that are used to differentiate an X-ray source as an AGN versus an SF galaxy, only one of the seven criteria needs to be satisfied for a source to be determined as an AGN. The majority of the criteria, as noted in Section 2, only capture moderate-to-high-power AGN, with the exception of the criterion that the full band X-ray luminosity is greater than 10^{42} [erg s^{-1}]. High-power AGN are rare in the small volume that the CDFS field probes, and thus the most common criteria the X-ray sources satisfy in L17 is the X-ray luminosity threshold. Due to our results indicating that a large fraction of sources may have X-ray luminosities underestimated by at least an order of magnitude, the objects in L17 that are classified as galaxies may also be obscured AGN.

In the entirety of the L17 catalog, 307 sources are classified as "galaxies." Of these 307 sources, we select objects with $z > 0.5$ and detections in the hard band (HB) in order to be consistent with the L17 classified AGN subsample. We use these objects in the analysis moving forward and label them as "galaxies." The galaxy subsample consists of 28 sources, where 80% have calculated rest-frame $L_{\text{Torus}*}$ values, 20% have uncorrected [O III] 5007λ luminosities greater than 10^{42} [erg s^{-1}], and 14% have VLA 1.4 GHz detections. Of the galaxy $L_{\text{Torus}*}$ subsample, 62% have both Herschel PACS detections and a mean and median 50 μm–to–5 μm luminosity ratio of 1.26 and 1.29, respectively.

In the following subsections, we estimate the potentially unaccounted-for obscuration and highlight some implications that might arise when one uses the most recent literature X-ray values for these objects.

4.2. Estimating the True Obscuration

We can estimate the level of obscuration by comparing the non-absorption-corrected X-ray luminosities to empirical studies utilizing the MIR wavelength measurements. In Figure 10, we determine where the non-absorption-corrected luminosities are located within empirically defined regions of nonobscured and heavily obscured sources, indicated by the
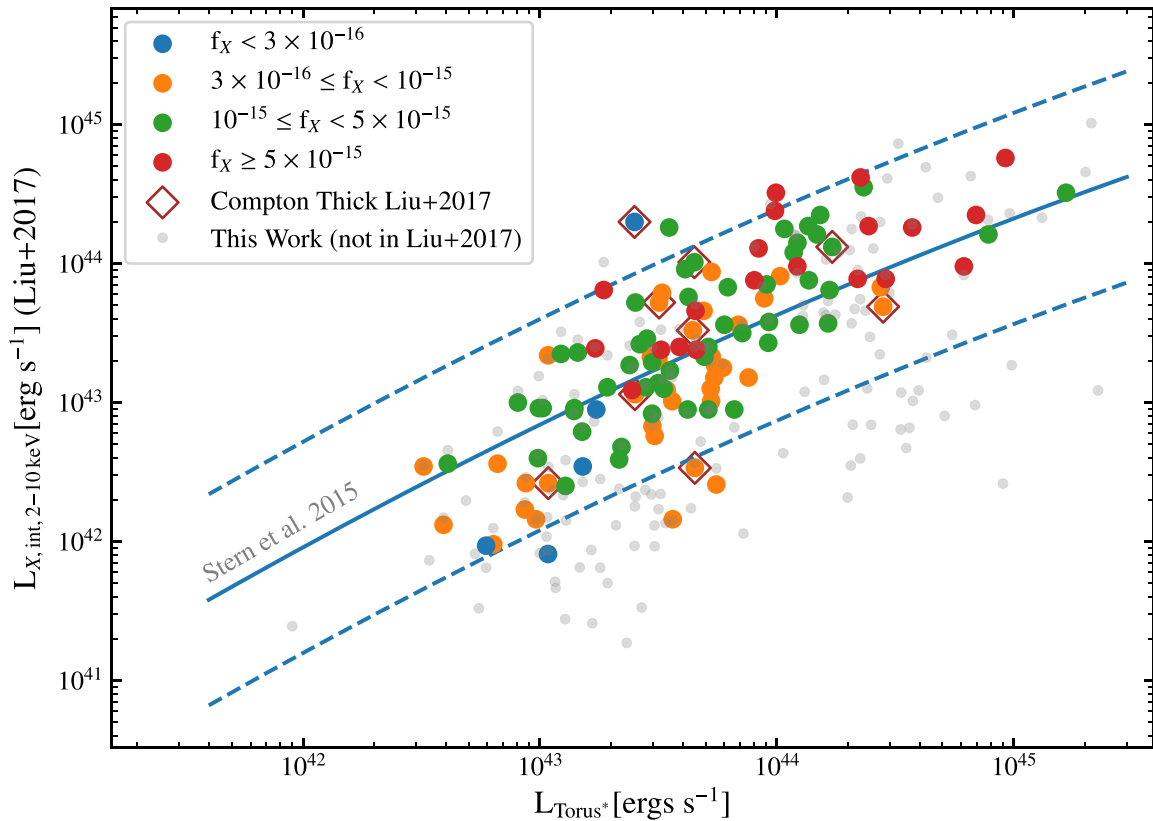
Figure 9. Shown is $L_{X,int,2-10\,keV}$ vs. L_{Torus^*}, where the absorption-corrected luminosities are provided from Liu et al. (2017). The points are color-coded by the X-ray flux provided in L17, and the fluxes have units of erg s^{-1} cm^{-2}. The blue solid line is the luminosity-dependent relationship from S15. Points surrounded by a red diamond are classified as Compton-thick in Liu et al. (2017). The gray points are the $L_{X,int,2-10\,keV}$ values from Figure 4 that did not have enough X-ray counts to be analyzed in Liu et al. (2017).

shaded regions. For the unobscured region, we use two different intrinsic X-ray$-6\ \mu$m AGN luminosity relationships: (i) the Gandhi et al. (2009) relationship, which was derived from a local sample of type 1 AGN and in which careful decomposition of the nuclear 6 μm luminosity was performed to minimize host-galaxy contamination, and (ii) the Fiore et al. (2009) relationship, which was derived from a sample that spanned a larger redshift and X-ray luminosity range as compared to Gandhi et al. (2009). The blue shaded region indicates the same relationships but where the X-ray luminosity is absorbed by a column density of $N_H = 10^{24}$ cm^{-2} as presented in Lansbury et al. (2015). For the objects with $f_X < 3 \times 10^{-16}$ erg s^{-1} cm^{-2}, 100% are below the empirically shaded region for unobscured AGN, and 74% are within or below the $N_H > 10^{24}$ cm^{-2} parameter space. Of these lowest flux objects, 70% have estimated N_H values that are an order of magnitude greater than the values derived from L17.

We then correct our $L_{X,int,2-10\,keV}$ values to account for the underestimation in N_H by assuming that (i) L_{Torus^*} is probing predominantly AGN processes and (ii) the lower 2σ value of the S15 relationship is a sufficient upper limit of the true intrinsic hard X-ray luminosity. For all objects that are $<2\sigma$ below the S15 relation in Figure 4, we compute the predicted X-ray luminosity for a given L_{Torus^*} value using the S15 relationship referenced in Section 3. We define these corrected luminosities as $L'_{X,int,2-10\,keV}$.

If our corrected luminosities are a better estimate of the intrinsic luminosity of these AGN, this implies that the hardness ratio (HR = (FH − FS)/(FH + FS)) for the faintest sources does not provide a correct indication of obscuration. As

detailed in Matt et al. (1997, 2000), a soft-scattered component of heavily obscured AGN can dominate at rest energies <10 keV. As we see in Figure 11, our most obscured sources live in the parameter space of moderate-to-high HRs. As shown in Brightman & Nandra (2012), the classical HR inference of heavily obscured sources may not be ideal. In L17, the majority of obscured sources do not have enough counts for detailed spectroscopic analysis; thus, the HR is used to estimate the N_H. In our work, we estimate how much the N_H would need to be corrected in order to correspond to empirical X-ray–IR relationships. In Figure 11, we combine the HRs, our estimated N_H (labeled as "N_H corrected"), and the X-ray–to–L_{Torus^*} ratio. We find that a fraction of the sources with the highest corrected N_H values have HRs (0–0.5) consistent with X-ray spectra that have a soft-scattered component (Brightman & Nandra 2012).

In the following sections, we explore the effect of these newly derived X-ray luminosities on two important features that are often considered when investigating the nature and evolution of AGN.

4.3. Implications for Radio-loudness Determination

About 10% of AGN have radio emission that is at least 10 times higher than one would expect from SF or other physical processes typical of the majority of AGN (Kellermann et al. 1989). These objects are known as radio-loud (RL) AGN.

A wealth of studies have argued for a bimodality in the distribution of radio-loudness parameters between jetted RL and nonjetted radio-quiet (RQ) AGN (Kellermann et al. 1989; Terashima & Wilson 2003; Padovani et al. 2017). These
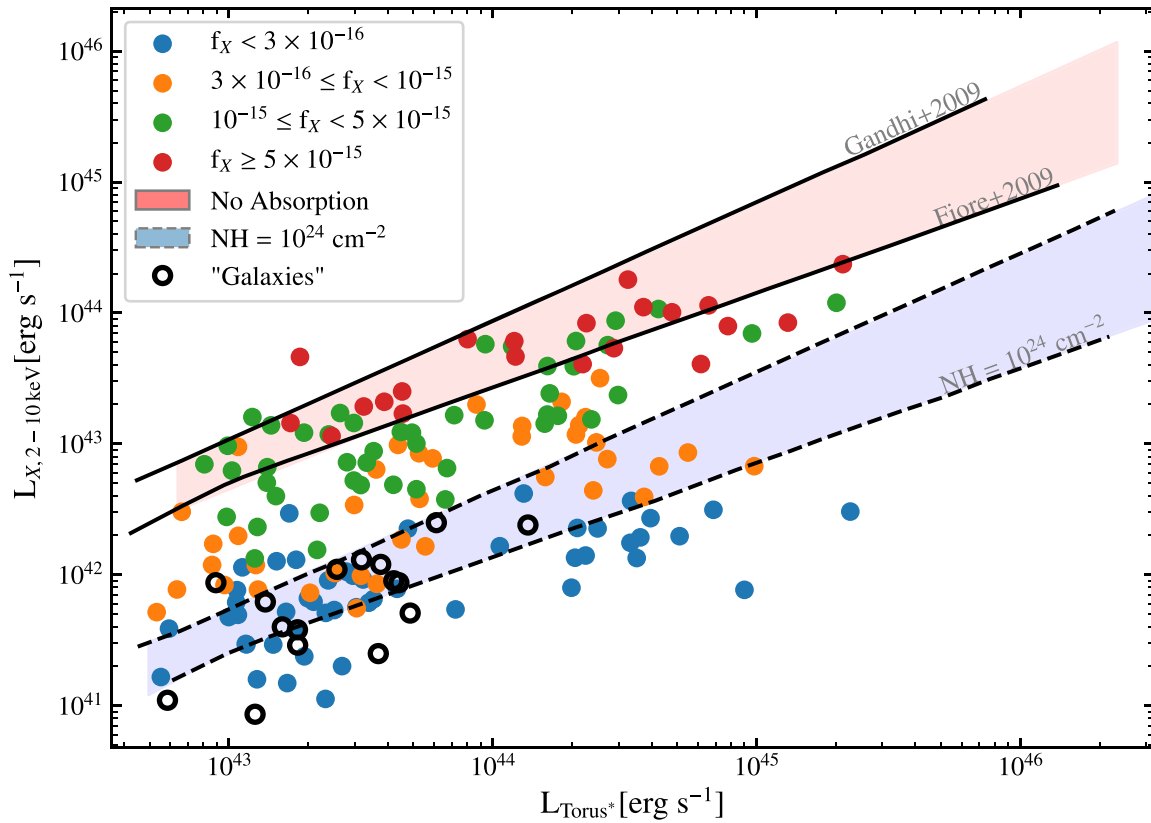
Figure 10. Non-absorption-corrected luminosities vs. L_{Torus^*}. The blue points have the lowest X-ray flux ($<3 \times 10^{-16}$ erg s^{-1} cm^{-2}). As adapted by Lansbury et al. (2015), the red shaded region indicates the range in intrinsic X-ray–6 μm AGN luminosity relationships between Gandhi et al. (2009) and Fiore et al. (2009). The blue shaded region indicates the same relationships but where the X-ray luminosity is absorbed by a column density of $N_H > 10^{24}$ cm^{-2} (Lansbury et al. 2015). The open black circles are L17 classified galaxies with $z > 0.5$ and a detection in the HB.
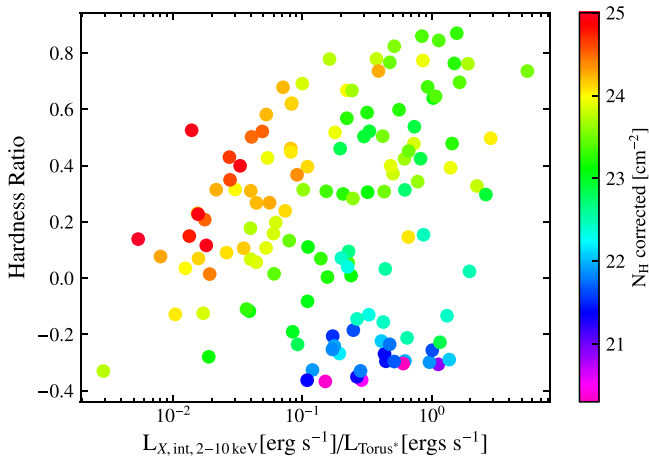
Figure 11. The HR as a function of $L_{X, int, 2-10\,keV}$ / L_{Torus^*}. The points are color-coded by our corrected N_H.

parameters define radio-loudness as the ratio between the radio luminosity and another luminosity measurement within the SED. With the aim of assessing the presence of an RL population in our sample, we first use the radio-loudness parameter as parameterized by the relationship between the radio and X-ray luminosities ($R_X = \nu L_{\nu, 1.4\,GHz}/L_{0.5-7\,keV}$; Terashima & Wilson 2003). This is relevant to this work because sources that are observed as underluminous in the X-ray with respect to their radio power could be mistakenly identified as RL AGN. If the dimming of X-ray flux due to the hypothesis of extra obscuration is correct, a large fraction of objects in our sample would be

erroneously classified as RL. In fact, a previous analysis of the 4 Ms CDFS AGN sample (Tozzi et al. 2009), which included only AGN with $L_{2-10} > 10^{42}$ erg s^{-1}, found that roughly 30% of their objects were RL.

The majority of our L17 subsample is not detected in the radio. In Figure 12, we show the distribution of the R_X for the 94 sources that are detected at 1.4 GHz (Luo et al. 2017). For ease of comparison to previous works, we calculate R_X using the absorption-corrected $L_{0.5-7\,keV}$ values provided in L17. We calculate the radio luminosities assuming a radio spectral slope of $\alpha = -0.7$, where $f_\nu \sim \nu^\alpha$. The dashed red line is the R_X threshold for radio-loudness as empirically determined in Terashima & Wilson (2003). The solid blue line is the median R_X value for the $z \approx 1$ 3C RL AGN sample (Wilkes et al. 2013), for reference. The 3C sample is used for comparison because these objects are bona fide RL AGN with robust X-ray measurements. The gray histogram is the distribution of the upper limit R_X for the sources in our sample with a radio upper limit. The radio upper limits are calculated using the limiting flux of the GOODS-S VLA survey (Miller et al. 2013). We also include the "galaxies" subsample, as indicated by the black histogram. According to the above assumptions, 56% of the radio-detected objects are classified as RL. This is significantly greater than the expected 10% (Terashima & Wilson 2003). Furthermore, in Figure 13, we find that the majority of objects posing as RL AGN are the sources in the two lowest flux bins.

Unless the X-ray measurements of our low-flux objects were not significantly underestimated, we would expect a radio-loudness analysis to yield similar number fractions to those found in other works. As seen in the lower panel of Figure 12,
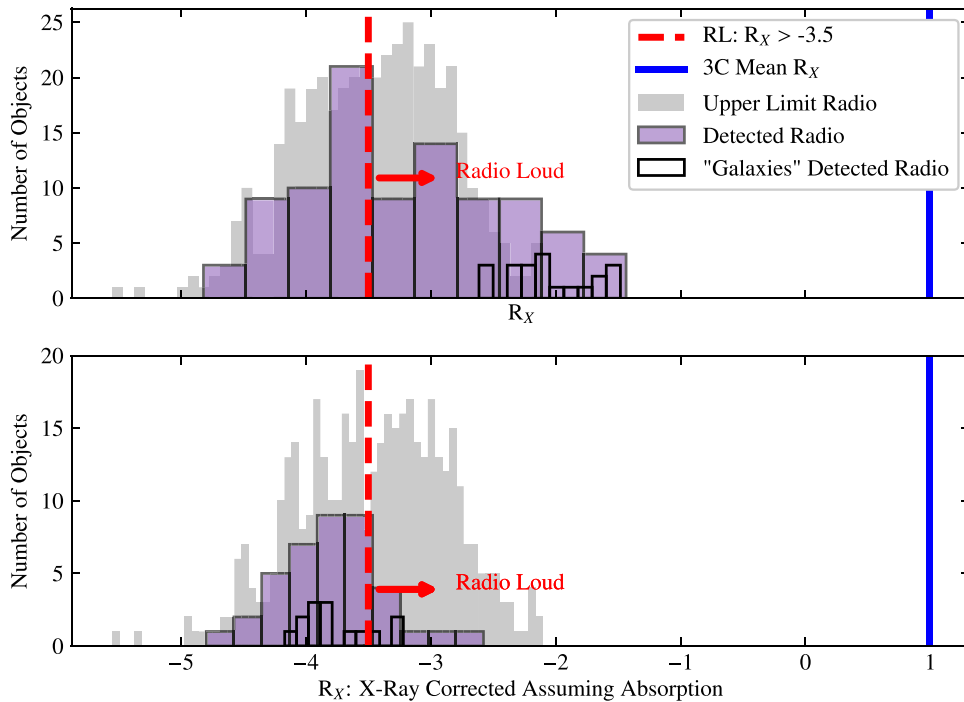
Figure 12. Radio/X-ray radio-loudness parameter distribution. In the top panel, we plot the distribution (dashed red line) of the radio-loudness diagnostic as parameterized by Terashima & Wilson (2003). We calculate the radio upper limits using the limiting flux of the GOODS-S VLA survey (Miller et al. 2013) and show the distributions of the upper limit R_X (gray). The dashed red line is the RL threshold as empirically found by Terashima & Wilson (2003). For comparison, the blue solid line is the mean R_X value for a sample of bona fide RL sources, namely the 3CR sample with $z > 1$ (Wilkes et al. 2013). In the lower panel, we compute the predicted X-ray luminosities for X-ray underluminous sources via the $L_{\mathrm{Torus^*}}$ values using the S15 relation. The black histogram is the distribution for the L17 classified galaxies with $z > 0.5$ and a detection in the HB.
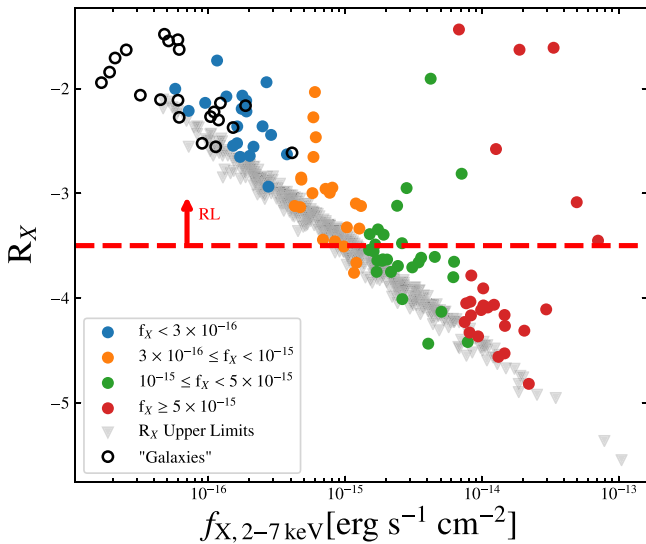
Figure 13. The R_X as a function of $f_{X,2-7\,\mathrm{keV}}$. The red line is the RL threshold as empirically found by Terashima & Wilson (2003), and the arrow indicates the region of radio-loudness. The open black circles are the L17 classified galaxies with $z > 0.5$ and a detection in the HB.

we find that the percentage of objects that are classified as RL is significantly reduced when using $L'_{\mathrm{X,int,2-10\,keV}}$: 13% of the 38 objects with radio, MIR, and X-ray detections. We believe that this constitutes a further indication that obscuration is present in a large fraction of these low X-ray flux sources, since this would explain the unreasonable fraction of RL objects observed if obscuration is not correctly taken into account.

We can also check radio-loudness using a diagnostic that does not rely on the X-ray detections. There are well-known

correlations between the IR and the radio (Sargent et al. 2010; Bonzini et al. 2012) that are expressed through the q_{24} parameter, which is the logarithm of the ratio between the IR and the radio flux density. Bonzini et al. (2012) parameterized the q_{24} parameter using the observed 24 μm flux density and 1.4 GHz radio flux density,

$$q_{24,\mathrm{obs}} = \log_{10}(S_{24\mu\mathrm{m}}/S_r), \qquad (1)$$

where $S_{24\,\mu\mathrm{m}}$ is the observed 24 μm flux density from MIPS and S_r is the observed 1.4 GHz flux density from the VLA. Observed flux densities are used, rather than rest-frame, due to insufficient data that are needed to derive bolometric values and avoid the high uncertainties that are introduced when modeling. Bonzini et al. (2012) assumed that the IR and radio properties of high-redshift star-forming galaxies are similar to local star-forming galaxies. Thus, a template of the prototypical starburst M82 is used to calculate $q_{24,\mathrm{obs}}$ as a function of redshift. We use the calculated M82 values as the star-forming galaxy locus via Bonzini et al. (2012) and classify objects that are RL as those with IR-to-radio fluxes that lie 2σ below the SF locus. In Figure 14, we color-code the $q_{24,\mathrm{obs}}$ values by whether they are classified as RL via R_X. We find significant disagreement between R_X and $q_{24,\mathrm{obs}}$. Note that only 8% of our sample is classified as RL when $q_{24,\mathrm{obs}}$ is used.

As seen in Figure 14, for the objects that are classified as RL using $L'_{\mathrm{X,int,2-10\,keV}}$ (red circles), there is 100% overlap with the $q_{24,\mathrm{obs}}$ diagnostic. Surprisingly, we also find an object within the "galaxies" subsample that is classified as an RL AGN in both the corrected R_X diagnostic and $q_{24,\mathrm{obs}}$. In summary, without the assumption that there is a significant
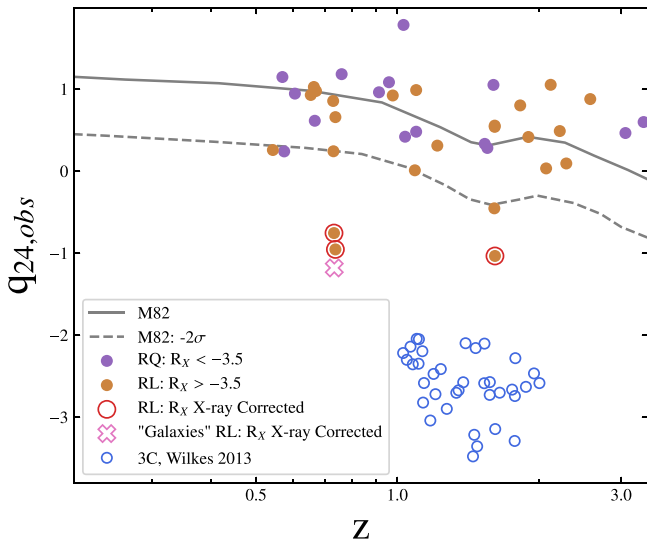
Figure 14. Shown is $q_{24,obs}$ as a function of redshift. The orange and blue circles represent the R_X RL and RQ, respectively. The dashed blue line is the lower 2σ evolution of $q_{24,obs}$ for M82 as plotted in Bonzini et al. (2012). The pink cross is an object within the L17 classified "galaxies" subset. We also plot the high-z 3C objects (Wilkes et al. 2013) for reference.

underestimation of the X-ray luminosity, over half of our sample would be erroneously classified as RL.

4.4. Implications for Obscured AGN Space Density

The results discussed in this paper also have important bearings for cosmological studies. A major implication of our finding is in fact related to the space density of obscured AGN. We estimate the space density for the obscured sources in our sample with and without the corrected X-ray luminosities. We use a binned luminosity function and define the three bins as $10^{42.5} < L_{X,2-10\,keV} \leqslant 10^{43.5}$, $10^{43} < L_{X,2-10\,keV} \leqslant 10^{44}$, and $10^{43.3} < L_{X,2-10\,keV} \leqslant 10^{44.3}$ with redshifts $0.5 < z \leqslant 1.0$, $1.0 < z \leqslant 1.5$, and $1.5 < z \leqslant 2.5$, respectively, where all luminosity units are in erg s^{-1}. In Figure 15, we show the intrinsic hard X-ray luminosity as a function of redshift for all sources with $N_H > 10^{24}$ cm^{-2} as defined by being within or below the blue shaded region in Figure 10. The blue points are corrected for additional obscuration as defined by $L'_{X,int,2-10\,keV}$. The open black circles are L17 classified galaxies. For comparison, we show the $L_{X,int,2-10\,keV}$ values (red crosses). We choose the luminosity–redshift bins to maximize the number of sources included in the calculation while minimizing the number of potential outliers. We immediately find that the difference between the $L_{X,int,2-10\,keV}$ and $L'_{X,int,2-10\,keV}$ values would have a significant effect on space density calculations. Furthermore, we can quantify this effect by comparing the space density of our most obscured sources to model expectations.

We take all of our objects with an estimated $N_H > 10^{24}$ cm^{-2} and calculate the space density of our heavily obscured sources in the CDFS field. We present two space densities per luminosity–redshift bin. The first is the AGN subsample presented in Figure 4, and the second includes these sources plus the objects in the "galaxies" subsample. We use a binned luminosity function as parameterized by Ranalli et al. (2016).

The differential luminosity function Φ is defined as the number of objects N at comoving volume V:

$$\Phi(L, z) = \frac{d^2N(L, z)}{dVdL}. \qquad (2)$$

We approximate the LF within a bin with luminosity boundaries $L_{min,2-10keV}$, $L_{max,2-10keV}$ and redshift boundaries z_{min}, z_{max} as N/V_{probed}, where V_{probed} is

$$V_{probed} = \int_{L_{min}}^{L_{max}} \int_{z_{min}}^{z_{max}} \Omega(L, z) \frac{dV}{dz} dz dL, \qquad (3)$$

dV/dz is the comoving volume, and $\Omega(L, z)$ is the survey coverage at the flux that an object of luminosity L would have if placed at redshift z.

In Figure 16, we show the space densities as a function of redshift for the three luminosity–redshift bins. The AGN-only subsample contains 19, 11, and 15 heavily obscured AGN candidates in the three redshift bins, respectively. The estimated space density of these objects within the redshift and luminosity bins are $6.9 \pm 1.5 \times 10^{-5}$, $2.5 \pm 0.9 \times 10^{-5}$, and $1.4 \pm 0.6 \times 10^{-5}$ Mpc^{-3}. The AGN + "galaxies" combined subsample contains 29, 14, and 16 objects for the three redshift bins. The estimated space densities of the "galaxies" combined subsample within the redshift and luminosity bins are $12.8 \pm 3.2 \times 10^{-5}$, $4.2 \pm 0.9 \times 10^{-5}$, and $1.5 \pm 0.6 \times 10^{-5}$ Mpc^{-3}. The errors include the upper and lower ends of the 68.3% confidence interval estimated using the standard Gehrels approximation (Gehrels 1986). We note that the x-axis errors in Figure 16 represent the range of the redshift bin used in the space density calculation. We find agreement with the predicted space density functions calculated using the X-ray background in Gilli et al. (2007). The models were based on the X-ray luminosity function observed at low redshift and parameterized with a luminosity-dependent density evolution. The Gilli et al. (2007) models were computed between the redshift and luminosity intervals referenced in Figure 16 and in the range 10^{24} cm$^{-2} < N_H < 10^{26}$ cm^{-2}. Compton-thick AGN that do not contribute to the X-ray background probed in Gilli et al. (2007), such as sources with low or zero scattering fractions or an obscuring medium that have a 4π covering factor, would not be represented; thus, these models represent lower limits.

The sources used to calculate the space densities in Figure 16 were measured to have $N_H > 10^{24}$ cm^{-2}; we estimate the error on this assumption by comparing the difference in space density estimates when using objects only below the shaded region to the values derived in Figure 16. We find a maximum 15% difference between including all of the objects in the blue shaded region versus only the objects below the blue shaded region.

We also estimate the number of AGN that may be missed in the 7 Ms CDFS via comparing to GOODS-S Spitzer/Herschel IR maps in this region (Elbaz et al. 2011). As seen in Donley et al. (2012), only 52% of IRAC AGN have X-ray counterparts in the 50–150 ks Chandra exposures. We check whether there is a significant portion of IRAC AGN lacking Chandra 7 Ms counterparts, for these may represent the most obscured AGN in the GOODS-S field. We first choose a subfield of the IRAC and Chandra GOODS-S images, where both maps overlap with one another. We then identify the IRAC AGN sources using the
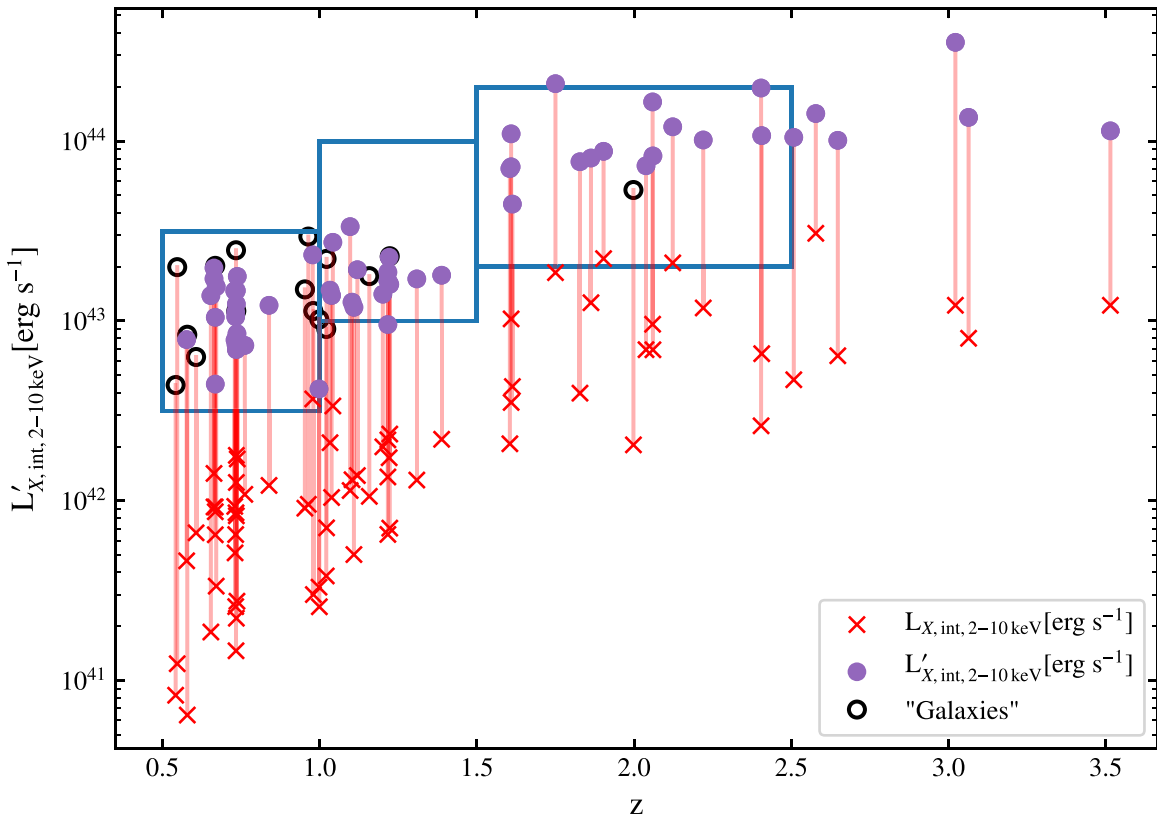
Figure 15. Binned luminosity function analysis. We show the intrinsic hard X-ray as a function of redshift for all sources with the $N_H > 10^{24}$ cm^{-2} parameter space defined in Figure 10. The blue points are corrected for additional obscuration as defined by $L'_{X,int,2-10\,keV}$. The open black circles are L17 classified galaxies. For comparison, we show the $L_{X,int,2-10\,keV}$ values (red crosses). The three rectangles are the three bins used in the luminosity function analysis.
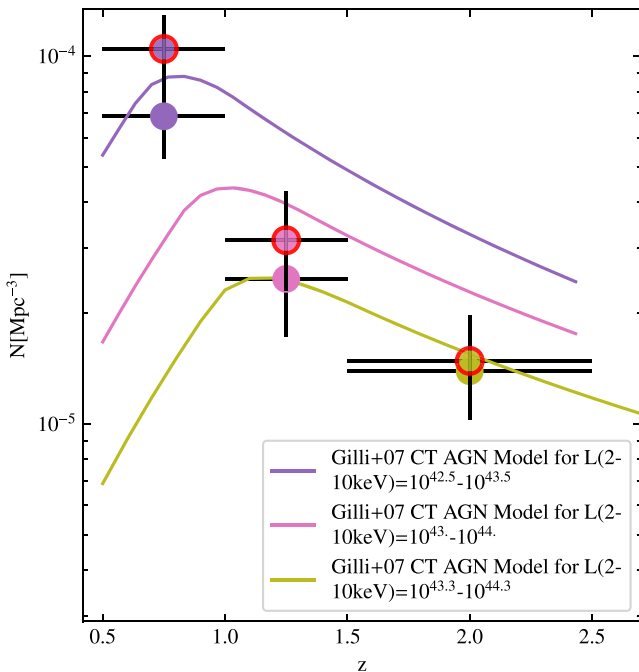

Figure 16. AGN space density. The filled points are the heavily obscured AGN space densities for each luminosity–redshift bin, and their colors correspond to the theoretical model values for that bin. The points circled in red are space density estimates including the L17 classified "galaxies" subsample. The errors include model error and the upper and lower ends of the 68.3% confidence interval estimated using the Gehrels approximation (Gehrels 1986). The solid lines are the expected functions for three luminosity bins as modeled by Gilli et al. (2007).

Donley et al. (2012) power-law AGN criteria, which are parameterized as follows: $x = log(f5.8/f3.6)$, $y = log(f8.0/f4.5)$ $x > 0.08\Lambda y > 0.15\Lambda y \geqslant (1.12 \times x) - 0.27\Lambda y \leqslant (1.12 \times x)\Lambda f4.5 > f3.6\Lambda f5.8 > f4.5\Lambda f8.0 > f5.8$ We find 48 power-law AGN in this IRAC GOODS-S subfield. We then one-to-one match these sources to the Chandra 7 Ms cutout using their GOODS-S IDs. We find 38 power-law AGN that also have a Chandra 7 Ms soft, full, and/or hard band detection. Thus, we find that 80% of IRAC AGN have an X-ray counterpart when compared to the significantly deeper 7 Ms exposure. While this shows that we may be missing 10 objects in this subfield due to lack of an X-ray detection, it also shows that the number of total AGN in the IR missed by the 7 Ms CDFS survey is within ∼20%. We are aware that this is still an incomplete assessment, for a more accurate estimate should take into account the different selection biases between the IR and X-ray catalogs. However, we remind the reader that the main goal of this paper is to improve upon characterizing the obscured AGN population for X-ray-selected sources.

Furthermore, the lowest and highest redshift bin space density enables us for the first time to make an accurate comparison with models in a parameter space poorly explored thus far. If we did not consider objects from the lowest X-ray flux bins as being obscured AGN, the estimated space density in the lowest redshift bin would drop by 50%, and the highest redshift bin would drop by 40%. By taking into account the results of our work, we are able to probe a fainter luminosity bin than previously estimated in the literature, and we find both heavily obscured AGN space density calculations consistent with the X-ray background models.

5. Summary and Conclusions

Utilizing the excellent wavelength coverage of the GOODS-S field, we compare the X-ray luminosities of AGN from the Chandra 7 Ms survey to the radio (VLA 1.4 GHz), optical grism spectroscopy (HST-WFC3), high-resolution optical/NIR imaging and photometry (HST-ACS, HST-WFC3IR), and NIR/MIR/FIR photometry (Spitzer IRAC, IRS PUI, and MIPS; Herschel PACS). We find that the lowest X-ray flux AGN ($f_X < 3 \times 10^{-16}$ erg s^{-1} cm^{-2}) in our sample have the greatest disagreement with their X-ray luminosities compared to their radio, IR, and optical counterparts.

We estimate the AGN contribution to the MIR by redshift-correcting the observed IRAC 8 μm, IRAC PUI 16 μm, and MIPS 24 μm fluxes for objects whose redshift corresponds to luminosities in the range between 3.2 and 5.7 μm. Of these objects, 44% are at least 2σ below the expected S15 relationship, which defines the relationship for absorption-corrected AGN in the MIR and X-ray.

The interpretation of these low-flux sources with underestimated X-ray luminosity is that a large column of obscuring material ($N_H > 10^{23}$ cm^{-2}) is attenuating the X-ray emission. Assuming these objects are indeed obscured AGN, we find that almost all of the lowest X-ray flux AGN in our L17 subsample have $N_H > 10^{24}$ cm^{-2}.

We explore the implications of our results and choose two examples where underestimated X-ray luminosities could affect AGN research. Using the radio diagnostics of Terashima & Wilson (2003) and Bonzini et al. (2012), 56% of our objects have an $L_{X,int,2-10\,keV}$ that would place them in the RL regime as compared to their 1.4 GHz radio emission. When we correct our X-ray luminosities for additional obscuration, only 13% of our objects are classified as RL. For the sources with an estimated $N_H > 10^{24}$ cm^{-2}, we calculate the heavily obscured AGN space density in the following luminosity–redshift bins: $10^{42.5} < L_{X,2-10\,keV} \leqslant 10^{43.5}$, $10^{43} < L_{X,2-10\,keV} \leqslant 10^{44}$, and $10^{43.3} < L_{X,2-10\,keV} \leqslant 10^{44.3}$ and redshifts $0.5 < z \leqslant 1.0$, $1.0 < z \leqslant 1.5$, and $1.5 < z \leqslant 2.5$, respectively. We find the heavily obscured AGN space densities for these bins to be $6.9 \pm 1.5 \times 10^{-5}$, $2.5 \pm 0.8 \times 10^{-5}$, and $1.4 \pm 0.4 \times 10^{-5}$ Mpc^{-3}. Our results are in agreement with models of the obscured AGN space density function as derived by Gilli et al. (2007).

Future work to test our estimation of the level of intrinsic obscuration can occur not only with future missions but also with currently operating telescopes. Using a large ground-based telescope, we can obtain more sensitive [O III] measurements, as well as other optical emission lines, to further probe the AGN power. In addition, we can use ALMA to characterize the dustiness of the host galaxies. This would test whether the unaccounted-for obscuration is truly located within parsecs of the SMBH versus host-galaxy obscuration (see Circosta et al. 2019; D'Amato et al. 2020 for further examples of this possibility). Future X-ray missions, such as ATHENA, will enable more sensitive X-ray measurements. This will allow for more rigorous spectral analysis of the low X-ray flux sources. Finally, the James Webb Space Telescope will allow us to directly image the MIR flux on kiloparsec scales. Thus, we can more robustly decouple SF from torus emission.

In conclusion, we find that a significant fraction of the low-flux population of Chandra 7 Ms AGN are obscured AGN in disguise. This population is usually missed and/or misclassified and should be taken into account when constructing AGN samples from deep X-ray surveys.

ORCID iDs

Erini L. Lambrides https://orcid.org/0000-0003-3216-7190
Marco Chiaberge https://orcid.org/0000-0003-1564-3802
Timothy Heckman https://orcid.org/0000-0001-6670-6370
Roberto Gilli https://orcid.org/0000-0001-8121-6177
Fabio Vito https://orcid.org/0000-0003-0680-9305
Colin Norman https://orcid.org/0000-0002-5222-5717

References

Akylas, A., Georgakakis, A., Georgantopoulos, I., Brightman, M., & Nandra, K. 2012, A&A, 546, A98
Alexander, D. M., Bauer, F. E., Chapman, S. C., et al. 2005, ApJ, 632, 736
Ananna, T. T., Treister, E., Urry, C. M., et al. 2019, ApJ, 871, 240
Armus, L., Charmandaris, V., Bernard-Salas, J., et al. 2007, ApJ, 656, 148
Asmus, D., Gandhi, P., Hönig, S. F., Smette, A., & Duschl, W. J. 2015, MNRAS, 454, 766
Asmus, D., Hönig, S. F., Gandhi, P., Smette, A., & Duschl, W. J. 2014, MNRAS, 439, 1648
Assef, R. J., Stern, D., Kochanek, C. S., et al. 2013, ApJ, 772, 26
Astropy Collaboration, Robitaille, E. J., & Tollerud, T. P. 2013, A&A, 558, A33
Blecha, L., Snyder, G. F., Satyapal, S., & Ellison, S. L. 2018, MNRAS, 478, 3056
Bonzini, M., Mainieri, V., Padovani, P., et al. 2012, ApJS, 203, 15
Bower, R. G., Benson, A. J., Malbon, R., et al. 2006, MNRAS, 370, 645
Brandt, W. N., & Hasinger, G. 2005, ARA&A, 43, 827
Brightman, M., & Nandra, K. 2012, MNRAS, 422, 1166
Brinchmann, J., Charlot, S., White, S. D. M., et al. 2004, MNRAS, 351, 1151
Brown, A., Nayyeri, H., Cooray, A., et al. 2019, ApJ, 871, 87
Buchanan, C. L., Gallimore, J. F., O'Dea, C. P., et al. 2006, AJ, 132, 401
Calzetti, D., Kennicutt, R. C., Engelbracht, C. W., et al. 2007, ApJ, 666, 870
Calzetti, D., Wu, S. Y., Hong, S., et al. 2010, ApJ, 714, 1256
Cattaneo, A., Blaizot, J., Devriendt, J., & Guiderdoni, B. 2005, MNRAS, 364, 407
Circosta, C., Vignali, C., Gilli, R., et al. 2019, A&A, 623, A172

Comastri, A., Ranalli, P., Iwasawa, K., et al. 2011, A&A, 526, L9
Comastri, A., Setti, G., Zamorani, G., & Hasinger, G. 1995, A&A, 296, 1
Croton, D. J., Springel, V., White, S. D. M., et al. 2006, MNRAS, 365, 11
Daddi, E., Alexander, D. M., Dickinson, M., et al. 2007, ApJ, 670, 173
D'Amato, Q., Gilli, R., Vignali, C., et al. 2020, A&A, 636, A37
Donley, J. L., Koekemoer, A. M., Brusa, M., et al. 2012, ApJ, 748, 142
Donley, J. L., Rieke, G. H., Pérez-González, P. G., & Barro, G. 2008, ApJ, 687, 111
Elbaz, D., Dickinson, M., Hwang, H. S., et al. 2011, A&A, 533, A119
Fabian, A. C. 1999, MNRAS, 308, L39
Fiore, F., Puccetti, S., Brusa, M., et al. 2009, ApJ, 693, 447
Gandhi, P., Horst, H., Smette, A., et al. 2009, A&A, 502, 457
Gehrels, N. 1986, ApJ, 303, 336
Gilli, R., Comastri, A., & Hasinger, G. 2007, A&A, 463, 79
Gilli, R., Salvati, M., & Hasinger, G. 2001, A&A, 366, 407
Heckman, T. M., & Best, P. N. 2014, ARA&A, 52, 589
Heckman, T. M., Ptak, A., Hornschemeier, A., & Kauffmann, G. 2005, ApJ, 634, 161
Hickox, R. C., & Alexander, D. M. 2018, ARA&A, 56, 625
Hickox, R. C., Myers, A. D., Greene, J. E., et al. 2017, ApJ, 849, 53
Hopkins, P. F., Hernquist, L., Cox, T. J., et al. 2006, ApJS, 163, 1
Hopkins, P. F., Hernquist, L., Cox, T. J., & Kereš, D. 2008, ApJS, 175, 356
Houck, J. R., Roellig, T. L., van Cleve, J., et al. 2004, ApJS, 154, 18
Houck, J. R., Soifer, B. T., Weedman, D., et al. 2005, ApJ, 622, L105
Hunter, J. D. 2007, CSE, 9, 90
Jones, E., Oliphant, T., Peterson, P., et al. 2001, SciPy: Open Source Scientific Tools for Python, http://www.scipy.org/
Kellermann, K. I., Sramek, R., Schmidt, M., Shaffer, D. B., & Green, R. 1989, AJ, 98, 1195
King, A. 2003, ApJL, 596, L27
Kirkpatrick, A., Pope, A., Alexander, D. M., et al. 2012, ApJ, 759, 139
Kirkpatrick, A., Pope, A., Charmand Aris, V., et al. 2013, ApJ, 763, 123
Kirkpatrick, A., Pope, A., Sajina, A., et al. 2015, ApJ, 814, 9
Lacy, M., Petric, A. O., Sajina, A., et al. 2007, AJ, 133, 186
Lacy, M., Storrie-Lombardi, L. J., Sajina, A., et al. 2004, ApJS, 154, 166
LaMassa, S. M., Heckman, T. M., Ptak, A., et al. 2010, ApJ, 720, 786
Lambrides, E. L., Petric, A. O., Tchernyshyov, K., Zakamska, N. L., & Watts, D. J. 2019, MNRAS, 487, 1823
Lansbury, G. B., Gandhi, P., Alexander, D. M., et al. 2015, ApJ, 809, 115
Liu, T., Tozzi, P., Wang, J.-X., et al. 2017, ApJS, 232, 8
Luo, B., Brandt, W. N., Xue, Y. Q., et al. 2017, ApJS, 228, 2
Madau, P., & Dickinson, M. 2014, ARA&A, 52, 415
Marchesi, S., Lanzuisi, G., Civano, F., et al. 2016, ApJ, 830, 100
Mateos, S., Alonso-Herrero, A., Carrera, F. J., et al. 2012, MNRAS, 426, 3271
Mateos, S., Alonso-Herrero, A., Carrera, F. J., et al. 2013, MNRAS, 434, 941

Matt, G., Fabian, A. C., Guainazzi, M., et al. 2000, MNRAS, 318, 173
Matt, G., Guainazzi, M., Frontera, F., et al. 1997, A&A, 325, L13
McKinney, W. 2010, in Proc. 9th Python in Science Conf., ed. S. van der Walt & J. Millman (Amsterdam: Elsevier), 51
Mignoli, M., Cimatti, A., Zamorani, G., et al. 2005, A&A, 437, 883
Miller, N. A., Bonzini, M., Fomalont, E. B., et al. 2013, ApJS, 205, 13
Momcheva, I. G., Brammer, G. B., van Dokkum, P. G., et al. 2016, ApJS, 225, 27
Mukai, K. 1993, Legacy, 3, 21
Mullaney, J. R., Pannella, M., Daddi, E., et al. 2012, MNRAS, 419, 95
Nenkova, M., Sirocky, M. M., Nikutta, R., Ivezić, Ž., & Elitzur, M. 2008, ApJ, 685, 160
Padovani, P., Alexander, D. M., Assef, R. J., et al. 2017, A&ARv, 25, 2
Pérez, F., & Granger, B. E. 2007, CSE, 9, 21
Persic, M., & Rephaeli, Y. 2002, A&A, 382, 843
Petric, A. O., Armus, L., Howell, J., et al. 2011, ApJ, 730, 28
Polletta, M., Weedman, D., Hönig, S., et al. 2008, ApJ, 675, 960
Ranalli, P., Comastri, A., Vignali, C., et al. 2013, A&A, 555, A42
Ranalli, P., Koulouridis, E., Georgantopoulos, I., et al. 2016, A&A, 590, A80
Sajina, A., Lacy, M., & Scott, D. 2005, ApJ, 621, 256
Sargent, M. T., Schinnerer, E., Murphy, E., et al. 2010, ApJ, 714, L190
Silk, J., & Mamon, G. A. 2012, RAA, 12, 917
Silk, J., & Rees, M. J. 1998, A&A, 331, L1
Silverman, J. D., Mainieri, V., Salvato, M., et al. 2010, ApJS, 191, 124
Skelton, R. E., Whitaker, K. E., Momcheva, I. G., et al. 2014, ApJS, 214, 24
Stern, D. 2015, ApJ, 807, 129
Stern, D., Assef, R. J., Benford, D. J., et al. 2012a, ApJ, 753, 30
Stern, D., Assef, R. J., Benford, D. J., et al. 2012b, ApJ, 753, 30
Stern, D., Eisenhardt, P., Gorjian, V., et al. 2005, ApJ, 631, 163
Stierwalt, S., Armus, L., Charmandaris, V., et al. 2014, ApJ, 790, 124
Symeonidis, M., Georgakakis, A., Page, M. J., et al. 2014, MNRAS, 443, 3728
Szokoly, G. P., Bergeron, J., Hasinger, G., et al. 2004, ApJS, 155, 271
Teplitz, H. I., Chary, R., Elbaz, D., et al. 2011, AJ, 141, 1
Terashima, Y., & Wilson, A. S. 2003, ApJ, 583, 145
Tozzi, P., Mainieri, V., Rosati, P., et al. 2009, ApJ, 698, 740
Treister, E., & Urry, C. M. 2005, ApJ, 630, 115
Weedman, D. W., Soifer, B. T., Hao, L., et al. 2006, ApJ, 651, 101
Weinberger, R., Springel, V., Pakmor, R., et al. 2018, MNRAS, 479, 4056
Wilkes, B. J., Kuraszkiewicz, J., Haas, M., et al. 2013, ApJ, 773, 15
Xue, Y. Q., Luo, B., Brandt, W. N., et al. 2011, ApJS, 195, 10
Yan, L., Donoso, E., Tsai, C.-W., et al. 2013, AJ, 145, 55
Yan, L., Sajina, A., Fadda, D., et al. 2007, ApJ, 658, 778
Yan, R., Ho, L. C., Newman, J. A., et al. 2011, ApJ, 728, 38